Innovative Cooling for Rocket Combustion Chambers

Jonas Peichl, Andreas Schwab, Markus Selzer, Hannah Böhrk, and Jens von Wolfersdorf

Abstract Transpiration cooling in combination with permeable ceramic-matrix composite materials is an innovative cooling method for rocket engine combustion chambers, while providing high cooling efficiency as well as enhancing engine life time as demanded for future space transportation systems. In order to develop methods and tools for designing transpiration cooled systems, fundamental experimental investigations were performed. An experimental setup consisting of a serial arrangement of four porous carbon fiber reinforced carbon (C/C) samples is exposed to a hot gas flow. Perfused with cold air, the third sample is unperfused in order to assess the wake flow development over the uncooled sample as well as the rebuilding of the coolant layer. Hereby, the focus is on the temperature boundary layer, using a combined temperature/pitot probe. Additionally, the sample surface temperature distribution was measured using IR imaging. The experiments are supported by numerical simulations which are showing a good agreement with measurement data for low blowing ratios.

1 Introduction

During the three funding periods (FP) of the TRR40 extensive investigations have been conducted in subproject A5 (SP A5) regarding transpiration cooling. Using detailed experimental analysis on single transpiration cooled samples, analytical 1D-models have been developed describing the cooling efficiency of the transpiration

J. Peichl (✉) · M. Selzer · H. Böhrk
DLR Institute of Structures and Design, Pfaffenwaldring 38-40, Stuttgart 70569, Germany
e-mail: jonas.peichl@dlr.de

A. Schwab · J. von Wolfersdorf
Institute of Aerospace Thermodynamics, Pfaffenwaldring 31, Stuttgart 70569, Germany

N. A. Adams et al. (eds.), *Future Space-Transport-System Components under High Thermal and Mechanical Loads*, Notes on Numerical Fluid Mechanics and Multidisciplinary Design 146, https://doi.org/10.1007/978-3-030-53847-7_3

cooled sample, but neglecting the coolant film development of upstream transpiration cooling (FP 1) [6]. To get a better understanding of the physical coupling mechanisms of the transpired coolant and the hot cross flow, the measurement apparatus was extended to measure the boundary layer characteristics using pitot tubes and thermocouples in the hot gas flow. Schlieren visualizations gave further insight into the interaction between coolant and hot gas flow [13]. The experimental data also served to validate numerical models coupling the hot gas flow and the porous wall [1, 8].

In contrast to film cooling, the pores in the material are very small and distributed over the surface. To be able to characterize this property, a test bench to measure this distribution has been developed, where the dynamic pressure distribution of the outflowing coolant is measured using a pitot tube [16]. Additionally, application of electro-coating processes allowed for improvements in the design of the samples [15]. This led to more robust samples, which made it possible to characterize fully instrumented samples and use these identical samples in the hot gas channel for transpiration cooling experiments. Thus, the effects of inhomogeneities in the outflow distribution on the cooling behaviour of the sample and the wake flow were demonstrated and even further incorporated into numerical results showing a good agreement in cooling behaviour [4]. Whilst the investigations in FP 1 and FP 2 have been focused on a single transpiration cooled sample, transpiration cooling offers the opportunity to adapt the local coolant mass flow by supplying different pressures, varying the porous wall thickness or stacking materials with different permeabilities. Thus, in a real combustion chamber an additional efficiency gain is expected by adjusting the coolant mass flow distribution to the local heat load and only replenishing the coolant film layed by upstream transpiration cooling as needed [2, 9, 10]. This concept is visualized in Fig. 1, depicting the approach of adjusting coolant mass flow to the local thermal situation.

Especially when taking into account the whole thrust chamber system with additional constraints like coolant supply pressure, injection temperature and highly varying thermal loads from injector to nozzle exit, it is evident that the most efficient cooling will be achieved by an optimized combination of different cooling techniques like transpiration-, film-, and regenerative cooling.

Using the combined approach of sample characterization, transpiration cooling experiments, analytical modelling and numerical simulations developed in FP 1 and FP 2, the current research is focused on local variations of coolant mass flow rate. Thereby, the effects of accumulating coolant film through transpiration cooling and degeneration of that film on low or non-perfused sections as well as replenishment of this coolant film can be studied in detail.

2 Experimental Setup

In order to experimentally determine the accumulation of coolant film and degeneration of the coolant layer over non-perfused samples, a new stacked ceramic test bed consisting of four independent samples has been developed. The specimen and

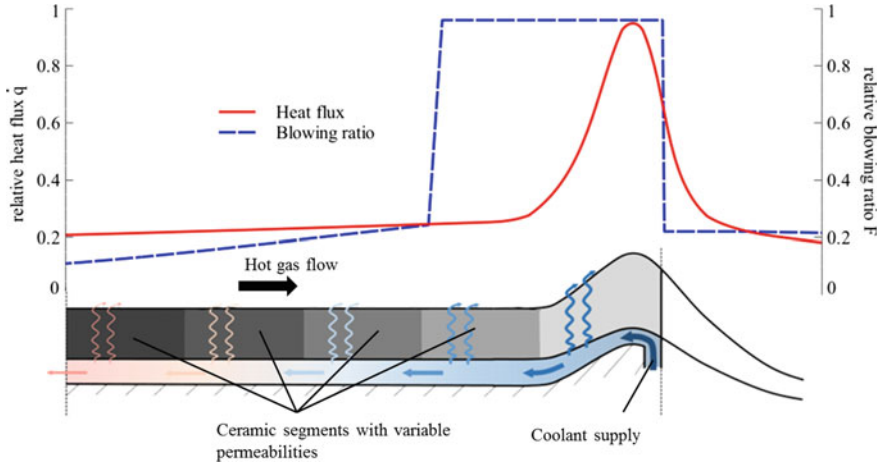

Fig. 1 Envisioned optimized cooling scheme for rocket combustion chambers

its characterization are described in Sect. 2.1. From preliminary numerical studies operating conditions have been identified that show the phenomena of accumulating coolant film, degeneration of the coolant film over a non-transpiration cooled section and subsequent regeneration of the coolant film [5]. The test channel and the operating conditions are described in Sect. 2.2.

2.1 Stacked Transpiration Cooling Specimen

The specimen shown in Fig. 2 contains four permeable Carbon/Carbon (C/C) samples of $A_C = L \times W = 67 \times 52\,\text{mm}^2$ size and $t = 10\,\text{mm}$ thickness each. Each of the samples exhibit a ply-parallel through-flow direction. Visible at the edges of the C/C samples, a galvanic copper layer is used to prevent lateral mass flow and to solder the individual sample into the sample holder. From the sample holder a 1 mm stainless steel plate can be seen at the leading and trailing edge. Additionally, to separate the coolant supplies of the four samples, a dividing plate is placed between each sample as shown in Fig. 2.

For temperature measurements ten Type K thermocouples are integrated into each sample. Four surface thermocouples at the outlet of the C/C-sample (see Fig. 2), one thermocouple at the backside surface and five thermocouples located at various depths inside the sample. These serve to capture the temperature distribution inside the C/C-samples when exposed to a hot gas flow. Each fully integrated and instrumented sample has been characterized at the AORTA (Advanced Outflow Research

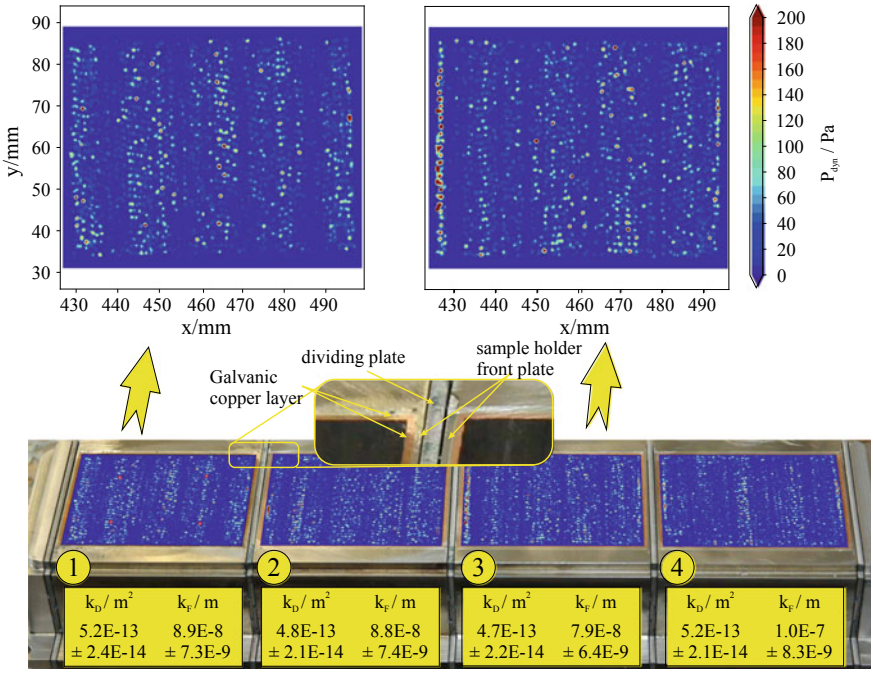

Fig. 2 Specimen setup and characterization

facility for Transpiration Applications) [16] test bench regarding permeability and outflow distribution.

Figure 2 shows the outflow distribution measured with a pitot tube with an inner diameter of 0.8 mm on a grid with a step size of 0.4 mm in x- and y-direction and a mass flow of 1.7 g/s. A detailed description of the measurement procedure is given in [15]. The contour graphs show the measured dynamic pressure at each point, where the colour scale has been adjusted to the same maximum value of 200 Pa, to best show the general outflow pattern. Typical for a ply-parallel through-flow are the line like patterns, stemming from the plies of the material as well as the regions with very little to no through-flow at the joints of the plates. This general pattern is similar for each sample, but the measurements also reveal some other outflow inhomogeneities between the samples. While sample 1 for example exhibits a homogeneous outflow distribution, sample 3 exhibits increased throughflow at the leading edge due to imperfections in the galvanic and soldering process.

The permeability of the samples is described by the Darcy-coefficient k_D and the Forchheimer-coefficient k_F, using the Darcy-Forchheimer equation in its compressible formulation given by Innocentini et al. [3] as

$$\frac{P_i^2 - P_o^2}{2P_o t} = \frac{\mu_o}{k_D} v_o + \frac{\rho_o}{k_F} v_o^2. \tag{1}$$

Thereby, P_i and P_o are the inlet and the outlet pressure. Further parameters are the thickness of the sample t, the dynamic viscosity of the coolant μ_o, the density of the fluid ρ_o and the superficial velocity v_o where the subscript $_o$ denotes values at the outlet of the sample. To determine the Darcy coefficient k_D and Forchheimer coefficient k_F, steady state measurements with different mass flow rates are conducted. The permeability coefficients are then fitted to the resulting pressure - massflow curve using a "least squares algorithm". The uncertainties are calculated using a Monte-Carlo method with a sample size of 200,000 [16]. With the current samples, measurements could be conducted with mass flows up to 10 g/s. The maximum pressures at 10 g/s ranges from 4.75 bar to 5.2 bar between the ceramic samples. The resulting permeability coefficients are also given in Fig. 2.

2.2 *Hot Gas Channel and Measurement Setup*

The described specimen is exposed to a hot gas flow within the Medium Temperature Facility (MTF). This suction mode driven test facility is heated up by an electrical heater and operating at test conditions of up to $T_{HG} = 373.15\,\text{K}$ for a maximum measurable mass flow rate of $\dot{m}_{HG} = 0.568\,\text{kg/s}$, a more detailed description is given in [12, 17]. Accelerated by a nozzle,the hot gas passes through a test section of a cross-section size of $A_{HG} = W\,x\,H = 60 \times 90\,\text{mm}^2$ and a final length of 290 mm [12, 14].

In order to obtain information about the boundary layer development above the effused porous samples a measurement rake is inserted in the test section with an axially and vertically traversable apparatus and depicted encircled in Fig. 3. A pitot tube ($0.5\,\text{mm} \pm 0.01$ OD, $0.3\,\text{mm} -0\ +0.02$ ID) for stagnation pressure measurements and a Type-K sheath thermocouple with a diameter of 0.5 mm recording a recovery temperature form a measurement rake which protrudes 20 mm oriented blunt into the undisturbed hot gas flow. Due to the inflow on the thermocouple, stem conduction caused measurement errors are neglectable small. A recalculation of the measured data into velocity and temperature profiles is done following the descriptions of [12]. In this investigation five different locations for temperature and velocity profile measurements have been chosen. The numbers 7, 8, 9, 10 and 12 in Fig. 3 refer to these measurement points at axial positions of 148 mm, 164 mm, 182 mm, 216 mm and

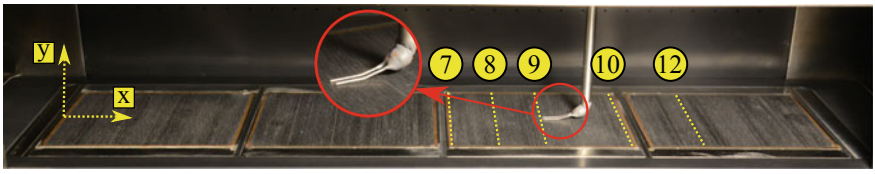

Fig. 3 Test section of the medium temperature facility and the various measuring positions for temperature and velocity boundary layers

Table 1 Summary of the derived steady-state test case parameters with the according inlet temperature and pressure

No.	$F_{C_{1,2,4}}$ / %	$\dot{m}_{C_{1,2,4}}$ / g/s	T_{S_2} / K	T_{S_3} / K	T_{S_4} / K	P_{S_1} / kPa	P_{S_2} / kPa	P_{S_4} / kPa
0	0.00	0.00	360.8	359.6	360.6	79.91	79.6	79.13
1	0.10	0.21	331.8	347.3	329.5	105.28	107.26	117.5
2	0.15	0.32	326.5	344.4	326.2	115.71	118.26	123.87
3	0.25	0.53	318.6	338.7	319.8	134.25	137.81	141.27
4	0.50	1.06	308.4	329.5	310.6	173.2	178.92	176.51
5	0.75	1.58	303.4	323.9	305.5	205.04	212.29	208.33
6	1.00	2.11	301.2	320.5	303.2	234.65	243.03	235.82
7	1.50	3.17	297.6	315.3	299.3	288.57	298.24	289.46

240 mm, respectively. These positions are selected due to the main objective of this measurement campaign as mentioned in Sect. 1 with an uncooled third sample, while samples 1, 2 and 4 are cooled by an identical mass flow of coolant air $\dot{m}_{C_{1,2,4}}$, varied for different testing conditions. Considering the mass fluxes of hot gas and transpired coolant through the porous samples the dimensionless blowing ratio

$$F_C = \frac{\text{transpired mass flux}}{\text{hot gas mass flux}} = \frac{\dot{m}_{C_{1-4}}/A_C}{\dot{m}_{HG}/A_{HG}} \tag{2}$$

can be defined. All steady state operating conditions are listed in details in Table 1.

In this context the pressures P_{S_i} represent the back plenum pressure in order to perfuse the various samples with their corresponding permeabilities according to Fig. 2 with the appropriate blowing ratios. Furthermore, the temperatures T_{S_i} pertain to the sample backside temperature, measured by thermocouples positioned on each sample back side. For T_{S_1}, the measurement data showed a significant deviation due to a loose contact to the sample. The measurement data are therefore omitted. Since for the boundary conditions for the simulation, as seen from plenum temperature measurements, no significant deviation has to be expected for sample 1, T_{S_1} is approached as T_{S_2}. On the outlet side the porous samples are exposed to main flow conditions at a hot gas temperature $T_{HG} = 373.15\,\text{K}$ and a hydraulic diameter based Reynolds number $\text{Re}_{D_h} = 200{,}000$. Knowing the test section cross size as well as the static channel pressure $p_{HG} = 80\,\text{kPa}$ inside the test section the hot gas mass flow amounts to $\dot{m}_{HG} = 0.327\,\text{g/s}$. This results in a bulk velocity of $u_{bulk} = 80\,\text{m/s}$ and a Mach number of $Ma = 0.2$ emphasizing incompressibility of the flow.

Besides boundary layer measurements with the measurement rake, the test section also provides optical access for an areal non-intrusive surface temperature measurement through a Calcium Fluoride window with a thickness of 5 mm. An infrared camera type FLIR SC7600 with a resolution of 640 × 512 pixels and sensitive for

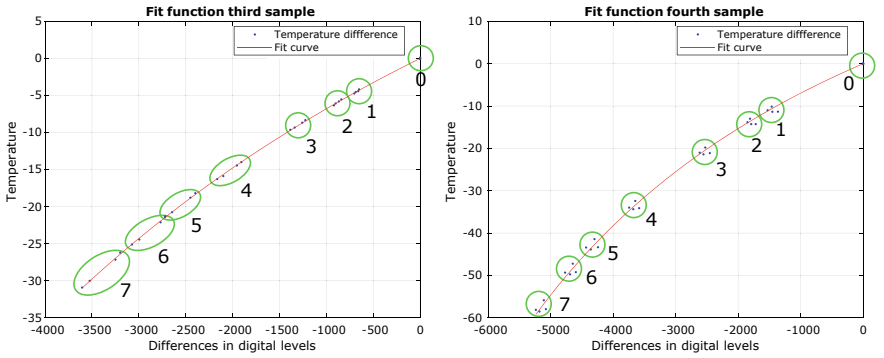

Fig. 4 Exemplary fit functions for transformation of recorded digital levels to a spatial temperature distribution for the third and fourth sample

wavelengths between 1.5 µm and 5 µm is installed aside the test section at an angle of $\alpha = 33°$ to the porous sample surface. In order to reduce optical warping the infrared camera is traversed parallel to the test section and focused on every sample's center axis individually resulting in four serial recordings per steady-state operational point in Table 1. For quantitative analysis of the infrared data an in-situ calibration according to Martiny et al. [7] with application of an empirical simplification of Planck's law is used. The latter one is fitted by a differential method on the basis of Prokein et al. [11] using the case without cooling, respectively number "0" in Table 1, as reference. This approach is visualized in Fig. 4 for the third and fourth ceramic sample.

For each test case the four surface thermocouples per sample as mentioned in Sect. 2.1 are correlated with the radiation intensity in direct vicinity of each thermocouple. Because of the high volumetric heat transfer coefficient, it is assumed that the porous wall and the coolant are in thermal equilibrium for this experimental setup [13]. Hence, the temperature measured by the thermocouples is roughly the wall temperature. Applying the differential method the latter ones are relating the surface temperature reductions to reductions of the measured radiation intensity recorded as Digital Levels, an intensity unit of the infrared camera linked to the chosen integration time. Thereby, external disturbances are eliminated due to the stationary operating points associated with constant disturbance.

3 Numerical Setup

For the simulation of transpiration cooled systems, numerical models were developed in cooperation with Dahmen et al. [1]. Thereon, a Computational Fluid Dynamics (CFD) design tool using the industry standard simulation software ANSYS CFX 17.2 has been developed. Latter one solves the Reynolds-averaged Navier–Stokes (RANS)

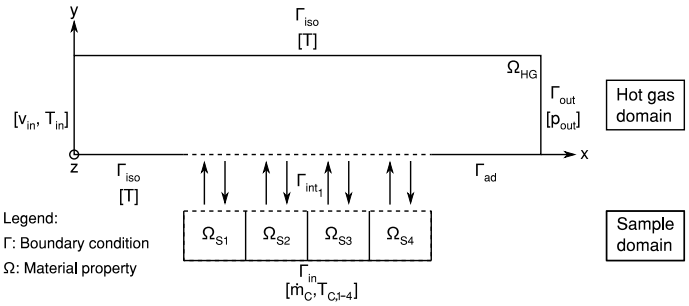

Fig. 5 Numerical setup

equations using a Finite-Volume method. The investigated problem is separated into two domains, representing the hot gas duct and the porous samples, respectively. Each domain is solved separately until local convergence is obtained. The results at the interface between the domains are transferred as boundary conditions, therefore coupling both domains externally via a Python script instead of a monolithic approach using ANSYS-internal coupling mechanisms. This approach has been validated using experimental data [8]. Global convergence is obtained when the difference of both temperatures at the interface reaches 0.1K.

For the hot gas domain, the given inlet boundary conditions are the measured inlet temperature and velocity profiles as well as the averaged outlet pressure provided by the vacuum pump [12]. The duct walls are either set as isothermal or adiabatic according to Fig. 5. Turbulence is modelled by the Shear Stress Transport (SST) turbulence model implemented in CFX, combining the κ-ω-model described by Wilcox [18] for the boundary layer region and the κ-ϵ-model for the free stream region. The iteratively changed boundary conditions provided by the porous domain are the sample surface temperatures $T_{PM,s}$ for the solid and $T_{PM,f}$ for the fluid as well as the outlet velocity vector $\overrightarrow{v}_{PM,out}$. The sample domain is modelled using the porous model implemented in CFX based on the Darcy-Forchheimer equation. The reservoir-side sample wall temperature boundary condition Γ_{in} is taken from experimental data according to Table 1, assuming thermal equilibrium between fluid and solid on the sample reservoir interface. The coolant mass flow is being calculated using the definition of the Blowing Ratio as given in Eq. 2, while assuming a fixed hot gas mass flow. On the duct side interface, the calculated heat flux stemming from the hot gas domain calculation is applied as a boundary condition $\Gamma_{int,1}$. The gaps between the samples are being modelled by setting a rather conservative thermal resistance of $3.84 \cdot 10^{-2}\,\mathrm{m^2 K\,W^{-1}}$ on the sample interfaces as described in [5].

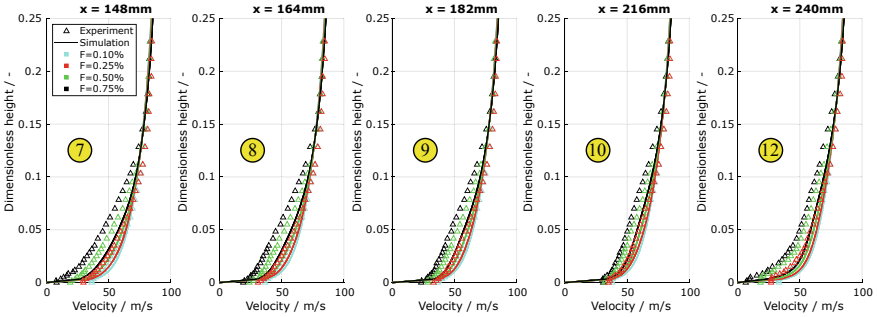

Fig. 6 Measured (symbol) and simulation (lines) velocity boundary profiles in streamwise direction at their corresponding axial position for various blowing ratios F in %

4 Results and Interpretation of the Serial Transpiration Cooling Experiment

The following section discusses the experimental and numerical results. In order to obtain an all-encompassing impression on the thermal situation in context of the non perfused ceramic sample, Fig. 7 illustrates the temperature boundary layer situation. Followed by an analysis of the surface temperature distribution measured by infrared thermography in Figs. 8 and 9, the temperature progression is continued with the sample-internal temperature distribution depicted in Fig. 10 assuming thermal equilibrium of fluid and solid. To complete the picture of the overall thermal structure a visualization of the fluid mechanical boundary layer situation is added in Fig. 6. As the comparison to the numerical simulations is the main purpose here, the presented data focuses mainly on cases 1, 3-5 described in Table 1, where the agreement is seen as acceptable. For higher blowing ratios additional investigations are needed.

In order to gain an overview of the overall fluid mechanical situation the velocity boundary layer profiles are shown in Fig. 6. Last mentioned are corrected in height by 0.3 mm as described in [12] because of placing the measuring probe under pretension near the wall. Visible in experimental data is an increase of near wall velocities due to a reduction of the coolant layer with increasing axial positions on top of the non cooled sample, until the fourth sample at $x = 240$ mm that is perfused again. However, the near wall measurements need to be considered carefully due to the finite dimension of the pitot tube with an outer diameter of 0.5 mm as described in Sect. 2.2. Nevertheless, a good agreement can be stated for the wall remote area in transition to the undisturbed free stream velocity in the channel center region with the numerical data. But in the range of the last 10–15% dimensionless distance to the wall the velocities differ significantly numerically predicting higher velocities in the velocity boundary layer. This mismatch motivates for a more profound insight of the mechanical boundary layer description and consequently needs to be investigated further.

Continuing on from that, the temperature profiles are also shown in Fig. 7 both experimentally and numerically up to a dimensionless channel height of 0.25. Addi-

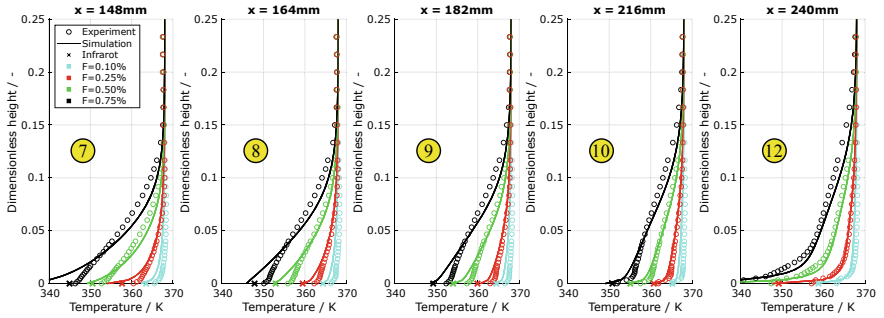

Fig. 7 Measured (symbol) and simulation (lines) temperature boundary profiles in streamwise direction at their corresponding axial position for various blowing ratios F in %

tionally, the surface temperatures, recorded by infrared thermography and averaged over a length of ±1mm in the direct vicinity of the five profile measurement points according to Fig. 3 in Sect. 2.2 along the median axis, are depicted in the temperature profile plots of Fig. 7 with a cross. It has to be noted that the agreement of the temperature profiles up to blowing ratios of $F = 0.5\%$ and a progressed axial position is quite decent. Even though three-dimensional channel side effects are neglected numerically, the difference of absolute values is rather small. However, the measured profiles show a slight kink between thickened boundary layer and non cooled, reheating wall, which is not visible in the simulated profiles. This experimentally measured thermal boundary layer behavior reflects the context of Fourier's law, considering the proportionality of heat flux and temperature gradient [13]. Due to missing coolant the heat flux into the wall is reduced in accordance with an increased surface wall temperature. Combined with a further increase of the thermal boundary layer thickness due to turbulent mixing effects within the hot gas flow, the kink occurs in the temperature profiles. Besides the numerically optimizable thermal boundary layer in the wake above the non-cooled ceramic sample, the boundary layer profiles of the cooled fourth sample are met well even for higher blowing ratios. Nevertheless, it has to be said, that also thermal near wall measurements need to be considered carefully due to the experimental setup explained in Sect. 2.2 with a measurement rake placed on the surface in contact to the wall with slight pretension. This and the extremely small size of the thermal viscous sublayer can further explain the discrepancy of the measured near wall temperatures and the infrared temperature data. Whereas the measured temperature profiles and the infrared thermography show slight differences to the numerical data the good agreement of the simulated data for blowing ratios up to $F = 0.5\%$ is even more remarkable. While at the beginning of the uncooled sample at a position of $x = 148$ mm the agreement is still rather poor, more downstream this agreement is convincing and is meeting the measured infrared surface temperatures perfectly.

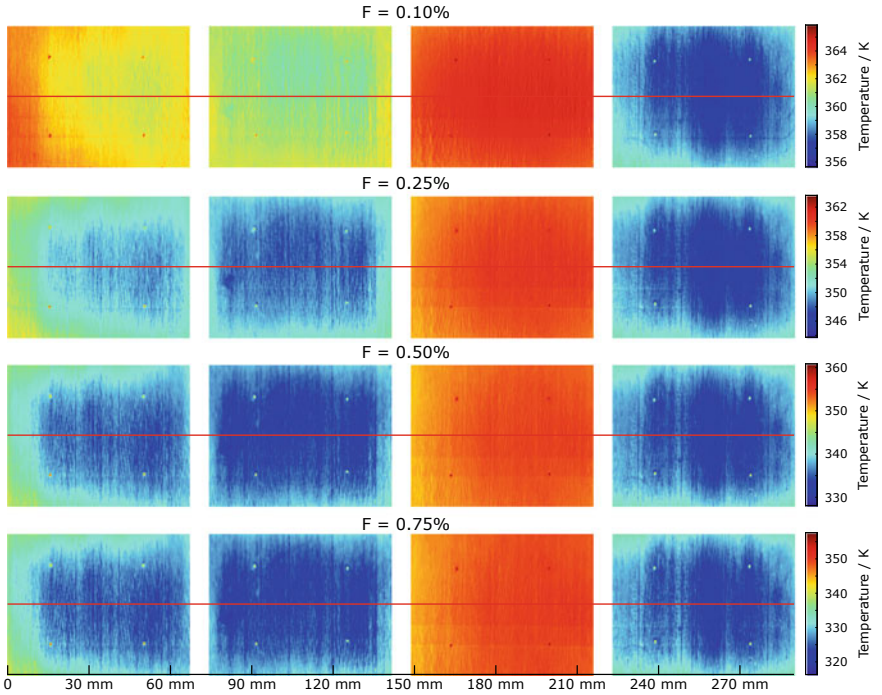

Fig. 8 Surface temperature distribution measured via infrared imaging (note different color scales per blowing ratio)

The temperature distribution on the sample surface determined via infrared imaging is shown in Fig. 8. For the perfused samples, it can be seen that the streamwise peripheral edges are at a higher temperature level compared to the sample center line, which is attributed to heat conduction from the hot channel walls. Further visible is a characteristic stripe pattern orthogonal to the flow direction which corresponds to the carbon fiber plies. The four thermocouples per sample used for calibrating the infrared camera as described in Sect. 2.2 can clearly be seen. The white spaces between the samples represent the non cooled metallic parts of the specimen, where the calibration of the infrared camera is not valid, and therefore no temperature data is available.

Due to the transpiration cooling, samples 1 and 2 are continuously cooled down, with across the gap could be observed, indicating that the gap has no significant influence on the cooling effect. In contrast, the trailing edge of sample 2 shows a slight increase of the surface temperature. For the non cooled sample 3, the surface temperature already increased over the gap and is further increasing over the first parts of the sample. While not reaching the temperature of the non cooled test case of $T_{S,uncooled} = 367\,\mathrm{K}$, the temperatures increase over the whole sample length. Especially for low blowing ratios, the temperature on sample 4 is almost immediately

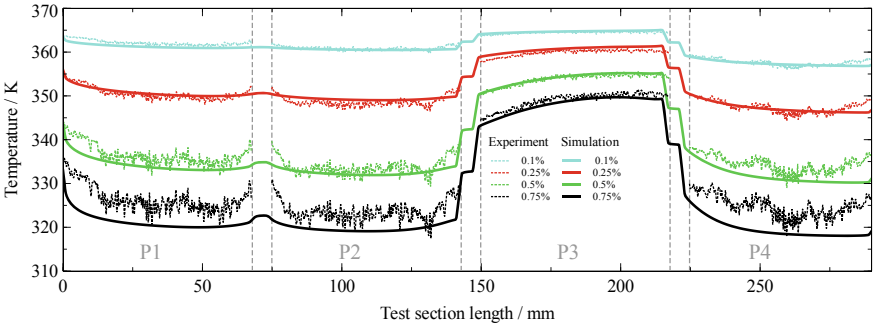

Fig. 9 Sample surface temperature distribution - measured data and numerical results

down or even below the temperatures of sample 2. The increase of the blowing ratio does only decrease the temperature level of the specimen.

In order to further investigate these effects, the surface temperature profiles along the sample center line marked red in Fig. 8 are depicted in Fig. 9 and compared to numerical simulations. Noticeable from these measurements, the amplitudes of the visible temperature oscillations are higher for the cooled samples compared to the uncooled sample. Comparing the experimental infrared temperature data to the simulated surface temperatures shows a good agreement. For low blowing ratios $F \leq 0.5\%$, the simulations match the cooling effect remarkably well on the first two samples as well as the third sample. In contrast, on the fourth sample the simulations overestimate the cooling effect. With increasing blowing ratios the simulations start to deviate from the measurement, as the cooling effect is significantly overestimated.

The measured sample-internal temperatures of samples 3 and 4 in comparison with the simulated sample temperature distribution are shown in Fig. 10. Subsequently focusing on the internal sample temperatures similar effects can be recognized. With the non perfusion of the third sample low temperature gradients through the channel height occur relatively to the much higher gradients in the cooled sample. This is directly related to the higher surface temperatures due to the kinking temperature profiles as explained above. In accordance with this, also on the backside a temperature gradient occurs. Despite a well isolated stack of samples, with heat conduction by the metallic mounting the entering compressed coolant of ambient air at ambient temperature is heated up and leads to a temperature layering within the sample back plenum. Comparing the simulation results to measurement data, the perfused sample 4 shows a significant deviation for blowing ratios of $F \geq 0.5\%$. For the unperfused sample, the simulated temperatures fit the measurement data for every investigated blowing ratio well.

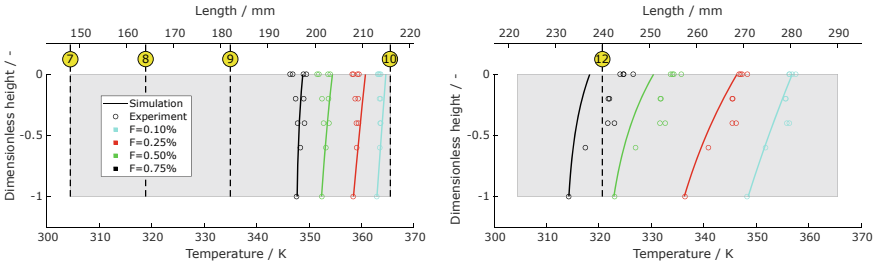

Fig. 10 Temperature profiles in porous samples 3 and 4 for various blowing ratios F

5 Summary and Outlook

The focus of the presented work was to investigate the cooling efficiency of a serial transpiration cooling arrangement. This was accomplished by setting up a serial arrangement of four identical CMC samples which could be independently perfused with cooling air. Measurements of the boundary layer were conducted using a measurement rake consisting of a pitot tube and a Type-K thermocouple. Additionally, the sample surface and internal temperature were measured using both thermocouples and infrared imaging. CFD simulations using ANSYS CFX were performed to support the experimental data. The cooling effect can be seen in infrared images. The described methods could be used to investigate the different phenomena linked with the cooling effect (coolant film, conduction in the specimen and sample internal heat transfer). Simulation results were compared with the experimental data, showing good agreement at low blowing ratios $F \leq 0.5\%$ for both flow temperature profiles and the surface temperatures provided by infrared measurement data. For higher blowing ratios, the numerical setup will be further improved in order to accurately simulate transpiration cooled systems.

In future investigations, the results will be transferred in an application-near environment, using the Sub-scale Validation Experiment (SVE), a cylindrical serial transpiration cooling experiment which is both capable of performing tests in a hot gas duct as well as using combustion processes in order to create an realistic environment comparable to rocket engine combustion chambers.

References

1. Dahmen, W., Müller, S., Rom, M., Schweikert, S., von Wolfersdorf, J.: Numerical investigations of transpiration-cooled turbulent channel flow. Int. J. Heat Mass Transf. pp. 90–100 (2015)
2. Eiringhaus, D., Riedmann, H., Knab, O., Haidn, O.J.: Full-scale virtual thrust chamber demonstrators as numerical testbeds within SFB-TRR 40. In: 2018 Joint Propulsion Conference, AIAA Propulsion and Energy Forum, Cincinnati, Ohio (AIAA 2018-4469), AIAA 2018-4469 (2018)

3. Innocentini, M.D., Pardo, A.R., Pandolfelli, V.C.: Influence of air compressibility on the permeability evaluation of refractory castables. J. Am. Ceram. Soc. **83**, 1536–1538 (2000)
4. König, V., Rom, M., Müller, S., Selzer, M., Schweikert, S., v. Wolfersdorf, J.: Numerical and experimental investigation of transpiration cooling with Carbon/Carbon characteristic outflow distributions. AIAA J. Thermophy. Heat Transf. **33**(2), 1–13 (2019)
5. Kromer, C.: Numerical investigations of coupling various cooling methods. ITLR, Universität Stuttgart, Master thesis, vol. 59 (2017)
6. Langener, T.: A contribution to Transpiration Cooling for Aerospace Applications Using CMC Walls. Ph.D. thesis, University of Stuttgart (2011)
7. Martiny, M., Schiele, R., Gritsch, M., Schulz, A., Wittig, S.: In Situ Calibration for Quantitative Infrared Thermography. QIRT 1996 - Eurotherm Series 50 - Edizioni ETS, Pisa 1997 (1996)
8. Munk, D., Selzer, M., Böhrk, H., Schweikert, S., Vio, G.: On the numerical modelling of transpiration-cooled turbulent channel flow with comparisons to experimental data. In: AIAA Journal of Thermophysics and Heat Transfer, to appear (2017)
9. Munk, D.J., Selzer, M., Steven, G.P., Vio, G.A.: Topology optimization applied to transpiration cooling. AIAA J. **57**(1), 297–312 (2019). https://doi.org/10.2514/1.J057411
10. Pfannes, P.: Numerisch gekoppelte Simulation einer Brennkammer mit neuartigen Köhlkonzepten. ITLR, Universität Stuttgart, Master thesis, vol. 75 (2018)
11. Prokein, D., von Wolfersdorf, J., Dittert, C., Böhrk, H.: Transpiration Cooling Experiments on a CMC Wall Segment in a Supersonic Hot Gas Channel. In: AIAA Propulsion and Energy Forum, International Energy Conversion Engineering Conference, Cincinnati, Ohio (2018)
12. Schwab, A., Peichl, J., Selzer, M., Böhrk, H., von Wolfersdorf, J.: Experimental Data of a Stacked Transpiration Cooling Setup with a Uniform Blowing Ratio. Sonderforschungsbereich/Transregio 40 - Annual Report 2016, 65-78 (2019)
13. Schweikert, S.: Ein Beitrag zur Beschreibung der Transpirationskühlung an keramischen Verbundwerkstoffen. Ph.D. Thesis, University of Stuttgart (2019)
14. Schweikert, S., Löhle, S., Selzer, M., Böhrk, H., von Wolfersdorf, J.: Surface heat flux determination of transpiration cooled C/C by the application of non integer system identification. In: Proceedings of the 8th European Workshop on Thermal Protection Systems and Hot Structures (2016)
15. Selzer, M., Schweikert, S., Böhrk, H., Hald, H., von Wolfersdorf, J.: Comprehensive C/C sample characterizations for transpiration cooling applications. Sonderforschungsbereich/Transregio 40 - Annual Report 2016, 61-72 (2016)
16. Selzer, M., Schweikert, S., Hald, H., von Wolfersdorf, J.: Throughflow characteristics of C/C. Sonderforschungsbereich/Transregio 40 - Annual Report 2014, 71-82 (2014)
17. Trübsbach, A., Schwab, A., Selzer, M., Böhrk, H., von Wolfersdorf, J.: Integration of a test setup for transpiration cooling. Sonderforschungsbereich/Transregio 40 - Annual Report 2018, 71-83 (2018)
18. Wilcox, D.C.: Turbulence Modeling for CFD. DCW Industries (2006)